Phase-field modeling by the method of lattice Boltzmann equations

Abbas Fakhari[1,2] and Mohammad H. Rahimian[2]
[1]*Hydraulic Machinery Research Institute, Faculty of Engineering, University of Tehran, Tehran, Iran*
[2]*Department of Mechanical Engineering, College of Engineering, University of Tehran, Tehran, Iran*
(Received 28 September 2009; revised manuscript received 30 December 2009; published 29 March 2010)

In this paper, at first, a lattice Boltzmann method for binary fluids, which is applicable at low viscosity values, is developed. The presented scheme is extension of the free-energy-based approach to a multi-relaxation-time collision model. Various benchmark problems such as the well-known Laplace law for stationary bubbles and capillary-wave test are conducted for validation. As an appealing application, instability of a rising bubble in an enclosed duct is studied and irregular behavior of the bubble is observed at very high Reynolds numbers. In order to highlight its capability to simulate high Reynolds number flows, which is a challenge for many other models, a typical wobbling bubble in the turbulent regime is simulated successfully. Then, in the context of phase-field modeling, a lattice Boltzmann method is proposed for multiphase flows with a density contrast. Unlike most of the previous models based on the phase-field theory, the proposed scheme not only tolerates very low viscosity values but also emerges as a promising method for investigation of two-phase flow problems with moderate density ratios. In addition to comparison to the kinetic-based model, the proposed approach is further verified by judging against the theoretical solutions and experimental data. Various case studies including the rising bubble, droplet splashing on a wet surface, and falling droplet are conducted to show the versatility of the presented lattice Boltzmann model.

DOI: 10.1103/PhysRevE.81.036707 PACS number(s): 47.11.−j, 47.55.dd

I. INTRODUCTION

Simulation of multiphase flows is a challenging task in the realm of computational fluid dynamics (CFD). Traditionally, one might solve the macroscopic Navier-Stokes equations (NSEs) that govern the physics of fluids together with a proper technique to track the interface between different phases. There are several interface-capturing methods such as the volume of fluid (VOF) method [1], front-tracking technique [2], and level set method [3]. The entire interface tracking and interface capturing schemes lie in two categories: sharp interface and diffuse interface models [4,5]. These conventional approaches may encounter numerical difficulties in capturing interface between different fluids whenever the rate of deformation is so high that the inception of interface breakup is very likely to happen.

As a diffuse interface approach, the lattice Boltzmann method (LBM) has emerged as an attractive computational scheme for simulation of multiphase flows, nonideal gases, and flow fields with complex geometries [6–10]. Phase segregation and interfacial dynamics, as well as employing various boundary conditions, which are difficult to deal with in the traditional methods, can easily be accounted for by the LBM via incorporation of intermolecular interactions and mesoscopic equations. On the other hand, the interface between different phases can be maintained automatically. It should be pointed that although the LBM is based on the mesoscopic kinetic equations, it arrives at solutions similar to those based on the solution of the NSE [6,11].

In the past decades, several LBMs for multiphase flow were proposed in the literature. The first multiphase LBM was proposed by Gunstensen *et al.* [12] and later modified by Grunau *et al.* [13]. This chromodynamic model uses red- and blue-colored particles to represent different fluids. In order to separate different phases, a recoloring step is introduced to force the colored particles to move toward fluids with the same color. The second model, also called the pseudopotential model, was proposed by Shan and Chen [14,15]. This model employs an interaction force between particles at neighboring lattice sites and is capable of simulating both miscible and immiscible fluids [16,17]. Based on a free-energy functional, Swift *et al.* [18] proposed the third class of multiphase LBMs. Unlike the pseudopotential model, the local momentum conservation is ensured, but this model does not satisfy Galilean invariance except for the case of binary ideal fluids [19,20]. All of the above-mentioned methods—in their primitive form—are restricted to low-density ratios around 1. A general description and weak points of these models can be found in the paper of He and Doolen [21]. Lately, He *et al.* [22] proposed a consistent multiphase LBM based on the kinetic theory for dense fluids, which was harnessed later [23] to study the Rayleigh-Taylor instability. Although this method is more robust than aforementioned models and yet more reliable and more powerful in study of droplet dynamics [24–26], it is restricted to density ratios up to about 15. Luo and Girimaji [27] also proposed an LBM for binary mixtures; nonetheless, we are not aware of any practical implementation of that model in study of multiphase flows.

Several researchers have attempted to apply the LBM at higher density ratios. Inamuro *et al.* [28] proposed a multiphase LBM in three dimensions (3D) that can tolerate large density differences. Their model must solve a Poisson equation for evaluation of pressure after imposing the incompressibility condition, which demands for much more computational time until convergence as the density ratio increases [29]. Therefore, most of their simulations were performed at a density ratio of 50. Another drawback of their model is that the mass conservation law is not satisfied because a cutoff value is used to determine the density of the fluid, similar to the level-set method [3]. Moreover, construc-

tion of the equilibrium distributions on a D3Q15 lattice instead of the D3Q19 or D3Q27 lattices may be another minor shortcoming of their method [30]. Lee and Lin [31,32] argued that the reason for instability of the kinetic-based LBM [22,23] at high-density ratios is the pressure gradient. By utilizing the idea of Jamet *et al.* [33] about the stress and potential forms of the surface-tension force, they proposed to discretize the gradient terms in different manners before and after streaming step. They employed a three-stage model together with stable discretization schemes to achieve a multiphase LBM applicable at high-density ratios. Nonetheless, in addition to its complexity and time-consuming nature, their model seems to be applicable in situations where the velocity and deformation rates are small [32]. However, in the real physical problems, such as falling [25] or moving droplet [26], the final velocity of the drop, and hence the inertial forces, should be high enough to allow for capturing different deformation and breakup modes [25,26]. Recently, Yuan and Schaefer [34] investigated the role of equation of state (EOS) in the second class of miscible multiphase LBMs [15,16] and expressed that the EOS plays an important role in achieving high-density ratios. More recently, Zheng *et al.* [35] proposed a multiphase method based on the free-energy approach. Their intention was to present an LBM applicable at high-density ratios, but their model deemed to be restricted to density-matched binary fluids as will be discussed later.

In general, different researchers reported diverse reasons for instability of the multiphase LBMs at high-density ratios. Some suspect the pressure gradients and discretization schemes [28,31], while others address the demand for a proper equation of state for multiphase flows at high-density ratios [21,34]. On the other hand, all of the aforementioned models use a single-relaxation-time Bhatnagar-Gross-Krook (BGK) model [36–38] in the collision process. Some deficiencies of the lattice BGK (LBGK) models are the inherent numerical instability as the relaxation time reaches 0.5 and a fixed Prandtl number (Pr=1). Recently, based on the idea of d'Humières [39], Lallemand and Luo [40] proposed a multiple-relaxation-time (MRT) collision operator for the lattice Boltzmann equation (LBE) models. The MRT-LBM, or the generalized LBE, overcomes some of the shortcomings of the LBGK such as a constant Prandtl number and fixed ratio between the kinematic and bulk viscosities [40]. From a computational point of view, the main advantage of the MRT model is its improved stability over the BGK scheme. The resulting technical merit of the MRT-LBM would be its ability to simulate fluid flows with very low viscosity values or, consequently, high Reynolds numbers, which is not attainable by the LBGK [41]. By applying optimization techniques in coding, the computational cost of the MRT-LBM will not be much higher than the BGK model [41].

Most of the existing MRT-LBE models are constructed and developed for the single-phase flows and few works are done with the MRT-LBM for multiphase flows [42], especially at high-density ratios [43]. Considering the importance of the multiphase flows in industrial processes and scientific researches, developing an MRT-LBM for two-phase flows with a density contrast is crucial. In the present study, in addition to a physical discussion, we will numerically show that the model of Zheng *et al.* [35] is nothing but a density-matched binary-fluid model. After developing the free-energy approach to an MRT collision model, we propose an LBM for multiphase flows based on the phase-field theory, which can tolerate very low viscosity values as well as different densities.

The rest of the paper is organized as follows. In Sec. II, the governing equations of the MRT-LBM for two immiscible fluids are described. Numerical results for this density-matched model are presented in Sec. III. This includes a variety of benchmarks for validation of the model, wobbling bubble at low Morton values, and turbulent flow in a Boussinesq fluid at extremely high Reynolds numbers. In Sec. IV, the governing equations of the phase-field MRT-LBM for multiphase flows is presented, followed by numerical verification in Sec. V. Then the scheme is invoked to study a more realistic rising bubble in a confined tube and the findings are compared to experimental data. To show the ability and accuracy of the model, two more real-world problems are considered: droplet splashing on a wet surface, in which an analytical solution for the spread radius is known, and a typical bag breakup of a falling droplet, which is compared to experimental observations. Both of the above case studies are further evaluated for accuracy and consistency by comparison to the kinetic-based LBM. Finally, the paper closes with a summary and conclusion in Sec. VI, with some suggestions for future works.

II. MRT-LBM FOR BINARY FLUIDS

In the diffuse interface modeling, the interface-capturing equation mimics the Cahn-Hilliard equation [44–49]

$$\frac{\partial \varphi}{\partial t} + \nabla \cdot (\varphi \mathbf{u}) = \theta_M \nabla^2 \mu_\varphi, \tag{1}$$

where t stands for the time, $\mathbf{u}$ is the macroscopic velocity, θ_M is the mobility, μ_φ is the chemical potential, and φ is the expected order parameter or phase field that tracks the interface. In the mean-field theory, the thermodynamic behavior of the fluid can be expressed by a free-energy functional of the form [44,49]

$$F = \int f(n, \varphi, \nabla \varphi) dV = \int \left[\psi(\varphi) + \frac{k}{2} |\nabla \varphi|^2 + nRTLn(n) \right] dV, \tag{2}$$

where R is the gas constant, T is the temperature, and n is the average number density

$$n = \frac{n_A + n_B}{2} \tag{3}$$

in which n_A and n_B are the densities of fluids A and B. In this study, the bulk free-energy density is chosen to have a double-well form [46,47]

$$\psi(\varphi) = a(\varphi^2 - \varphi^{*2})^2, \tag{4}$$

where φ^* is a constant that corresponds to the equilibrium state of the bulk free energy, $\varphi = \pm \varphi^*$, and defines by

$$\varphi^* = \frac{n_A - n_B}{2}. \tag{5}$$

The parameters a and k are related to the surface tension and interface width, respectively, by [46,47]

$$\sigma = \frac{4\sqrt{2ka}}{3}\varphi^{*3}, \tag{6}$$

$$W = \frac{\sqrt{2k/a}}{\varphi^*}, \tag{7}$$

and the order-parameter profile along the direction normal to a flat interface z is given by [47]

$$\varphi = \pm \varphi^* \tanh\left(\frac{2z}{W}\right). \tag{8}$$

The chemical potential could be written as

$$\mu_\varphi = 4a\varphi(\varphi^2 - \varphi^{*2}) - k\nabla^2\varphi. \tag{9}$$

A. MRT-LBE for interface-capturing equation

Zheng *et al.* [35] used a D2Q5 lattice structure for the interface-capturing equation. They stated that it is not necessary for interface-capturing equation to be fourth-order isotropic and the D2Q5 model is sufficient to capture the position of the interface. However, we utilize the D2Q9 lattice here. Although it may increase the computational time, the order parameter, which is used to track the interface between different phases, can be resolved better in a D2Q9 lattice. Moreover, even though the D2Q5 model has proved to be adequate for tracking the interface [46], it cannot deal with various boundary conditions (BCs) accurately. For example, there is no difference between the nonslip and free-slip BCs in a D2Q5 lattice structure; therefore, we continue with the nine discrete velocities in the D2Q9 model [11,38]

$$\mathbf{e}_\alpha = \begin{cases} (0,0) & \alpha = 0 \\ c(\cos\theta, \sin\theta), & \theta = (\alpha-1)\pi/2, \quad \alpha = 1,2,3,4 \\ \sqrt{2}c(\cos\theta, \sin\theta), & \theta = (\alpha-5)\pi/2 + \pi/4, \quad \alpha = 5,6,7,8, \end{cases} \tag{10}$$

where $c = \delta_x/\delta_t$ is the lattice velocity. The generalized LBE for the interface-capturing equation may be written as

$$f_\alpha(\mathbf{x} + \mathbf{e}_\alpha\delta_t, t + \delta_t) = f_\alpha(\mathbf{x}, t) - S_{\alpha i}(f_i - f_i^{eq}), \tag{11}$$

where f_α is the order-parameter distribution function and $S_{\alpha i}$ are elements of the general 9×9 collision matrix $\mathbf{S}$ in velocity space [40]. In the LBGK model, $\mathbf{S}$ is a diagonal matrix with the elements being $1/\tau$, where τ is the conventional single relaxation parameter. Also note that the summation convention for repeated indices is assumed here.

The chemical potential will be included in the LBE through the equilibrium distribution function. For the D2Q9 lattice, the equilibrium distribution is given by [48]

$$f_\alpha^{eq} = \begin{cases} \varphi - 3\mu_\varphi\Gamma(1 - w_0), & \alpha = 0 \\ 3w_\alpha[\mu_\varphi\Gamma + \varphi(\mathbf{e}_\alpha \cdot \mathbf{u})], & \alpha = 1-8. \end{cases} \tag{12}$$

The weight coefficients in the D2Q9 lattice are $w_0 = 4/9$, $w_{1-4} = 1/9$, and $w_{5-8} = 1/36$ [11,38].

Equation (11) might be recast in the following form:

$$f_\alpha(\mathbf{x} + \mathbf{e}_\alpha\delta_t, t + \delta_t) = f_\alpha(\mathbf{x}, t) - M_{\alpha i}^{-1}\hat{S}_{ik}(\hat{f}_k - \hat{f}_k^{eq}), \tag{13}$$

in which $M_{\alpha i}$ are elements of an invertible matrix transforming the distribution functions in velocity space into their counterparts in moment space and vice versa

$$\hat{f}_\alpha = M_{\alpha i}f_i; \quad \hat{f}_\alpha^{eq} = M_{\alpha i}f_i^{eq},$$

$$f_\alpha = M_{\alpha i}^{-1}\hat{f}_i; \quad f_\alpha^{eq} = M_{\alpha i}^{-1}\hat{f}_i^{eq}. \tag{14}$$

The diagonal relaxation matrix in moment space is given by

$$\hat{S} = MSM^{-1} = \mathrm{diag}(s_1, s_2, s_3, s_4, s_5, s_6, s_7, s_8, s_9), \tag{15}$$

where the coefficients s_{1-9} are the inverse of the relaxation rates. The parameter s_8 determines the viscosity of the fluid by

$$\nu = \frac{1}{3}\left(\frac{1}{s_8} - \frac{1}{2}\right). \tag{16}$$

Also, the following relation is established by Lallemand and Luo [40]:

$$s_5 = 3\left(\frac{2 - s_8}{3 - s_8}\right). \tag{17}$$

The transformation matrix is explicitly given by [40]

$$\mathbf{M} = \begin{bmatrix} 1 & 1 & 1 & 1 & 1 & 1 & 1 & 1 & 1 \\ -4 & -1 & -1 & -1 & -1 & 2 & 2 & 2 & 2 \\ 4 & -2 & -2 & -2 & -2 & 1 & 1 & 1 & 1 \\ 0 & 1 & 0 & -1 & 0 & 1 & -1 & -1 & 1 \\ 0 & -2 & 0 & 2 & 0 & 1 & -1 & -1 & 1 \\ 0 & 0 & 1 & 0 & -1 & 1 & 1 & -1 & -1 \\ 0 & 0 & -2 & 0 & 2 & 1 & 1 & -1 & -1 \\ 0 & 1 & -1 & 1 & -1 & 0 & 0 & 0 & 0 \\ 0 & 0 & 0 & 0 & 0 & 1 & -1 & 1 & -1 \end{bmatrix}. \tag{18}$$

From a computational viewpoint, it is strictly recommended to avoid matrix calculations [41]. Hence, we multiply Eq. (13) by the transformation matrix $\mathbf{M}$ to get to the following MRT-LBM for interface-capturing equation

$$\hat{f}_\alpha(\mathbf{x} + \mathbf{e}_\alpha\delta_t, t + \delta_t) = \hat{f}_\alpha(\mathbf{x}, t) - \hat{S}_{\alpha i}(\hat{f}_i - \hat{f}_i^{eq}). \tag{19}$$

The order parameter is computed after the streaming step by

$$\varphi = \sum_{\alpha=0}^{8} f_\alpha. \tag{20}$$

B. MRT-LBE for hydrodynamic equations

The NSE for the density-matched binary mixtures may be written as

$$n\frac{D\mathbf{u}}{Dt} = -\nabla\cdot\mathbf{P} + \mu\nabla^2\mathbf{u} + \mathbf{F}_b, \tag{21}$$

where $\mathbf{P}$ is the pressure tensor, μ is the dynamic viscosity, and $\mathbf{F}_b$ is the body force. It should be pointed that, as it is tacitly assumed, the number densities of the different fluids could not have noticeable difference; otherwise the average number density in Eq. (3) is not meaningful anymore. Moreover, from previous studies [20,49], we know that the total number density remains unchanged in the whole fluid; hence, n in Eq. (21) is constant. This is why the model of Zheng *et al.* [35] is not capable of simulating multiphase flow with large density ratios.

Similar to the evolution equation for the interface tracking distribution function, the LBE for evaluating hydrodynamic properties such as the number density and velocity reads as

$$g_\alpha(\mathbf{x}+\mathbf{e}_\alpha\delta_t, t+\delta_t) = g_\alpha(\mathbf{x},t) - S_{\alpha i}(g_i - g_i^{eq}) + F_\alpha - \frac{1}{2}S_{\alpha i}F_i, \tag{22}$$

where F_α is the forcing term in velocity space

$$F_\alpha = \frac{w_\alpha}{c_s^2}\left[(\mathbf{e}_\alpha - \mathbf{u}) + \frac{(\mathbf{e}_\alpha\cdot\mathbf{u})}{c_s^2}\mathbf{e}_\alpha\right]\cdot(\mathbf{F}_b + \mathbf{F}_s) \tag{23}$$

and

$$\mathbf{F}_s = \mu_\varphi\nabla\varphi \tag{24}$$

is the surface-tension force. The equilibrium distributions are given by [48]

$$g_\alpha^{eq} = \begin{cases} nw_0\left(1-\frac{3}{2}u^2\right) - 3(1-w_0)\varphi\mu_\varphi, & \alpha = 0 \\ w_\alpha\left[3\varphi\mu_\varphi + n\left(1+3\mathbf{e}_\alpha\cdot\mathbf{u}+\frac{9}{2}(\mathbf{e}_\alpha\cdot\mathbf{u})^2 - \frac{3}{2}u^2\right)\right], & \alpha = 1-8. \end{cases} \tag{25}$$

In the framework of the MRT-LBM, the distribution function in moment space becomes

$$\hat{g}_\alpha(\mathbf{x}+\mathbf{e}_\alpha\delta_t, t+\delta_t) = \hat{g}_\alpha(\mathbf{x},t) - \hat{S}_{\alpha i}(\hat{g}_i - \hat{g}_i^{eq}) + \hat{F}_\alpha - \frac{1}{2}\hat{S}_{\alpha i}\hat{F}_i, \tag{26}$$

where $\hat{g}_\alpha$ and $\hat{F}_\alpha$ are the distribution function and forcing term, respectively, in moment space (see the Appendix). The macroscopic properties are calculated after the advection step

$$n = \sum_{\alpha=0}^{8} g_\alpha, \tag{27}$$

$$n\mathbf{u} = \sum_{\alpha=1}^{8} g_\alpha\mathbf{e}_\alpha + \frac{(\mathbf{F}_b+\mathbf{F}_s)}{2}\delta_t. \tag{28}$$

Notice that unlike the pseudopotential method [16], the forcing term conserves the momentum exchange at each lattice site because $\mathbf{F}_b$ and $\mathbf{F}_s$ are nothing but the external body force and the continuous surface-tension force in the two-phase NSE.

III. NUMERICAL IMPLEMENTATION

In the present study, the values of s_1, s_4, and s_6 are set equal to unity. Also we have $s_8 = s_9 = 1/\tau$. The remaining two relaxation parameters, s_3 and s_7, can be adjusted arbitrarily.

A. Stationary bubble test

As a common task in verification of multiphase models, the well-known Laplace test for static bubbles is conducted and the results are compared to the theoretical solution. According to the Laplace law, the pressure difference across the interface of a two-dimensional (2D) bubble at equilibrium is related to the surface tension via

$$\Delta p = p_{in} - p_{out} = \frac{\sigma}{R}, \tag{29}$$

where R is the radius of the bubble. The pressure p in the free-energy model is related to the pressure tensor by [6,18,21]

$$P_{ij} = p\delta_{ij} + kn_{,i}n_{,j}. \tag{30}$$

Besides, the following thermodynamic relation holds [6,21]:

$$p = \varphi\frac{\delta F}{\delta\varphi} - F = p_0 - k\varphi\nabla^2\varphi - \frac{k}{2}|\nabla\varphi|^2 + nRT, \tag{31}$$

where

$$p_0 = \varphi\frac{d\psi}{d\varphi} - \psi \tag{32}$$

is the EOS [6,20]. Thus, the pressure reads as

$$p = a(3\varphi^4 - 2\varphi^2\varphi^{*2} - \varphi^{*4}) - k\varphi\nabla^2\varphi - \frac{k}{2}|\nabla\varphi|^2 + nRT. \tag{33}$$

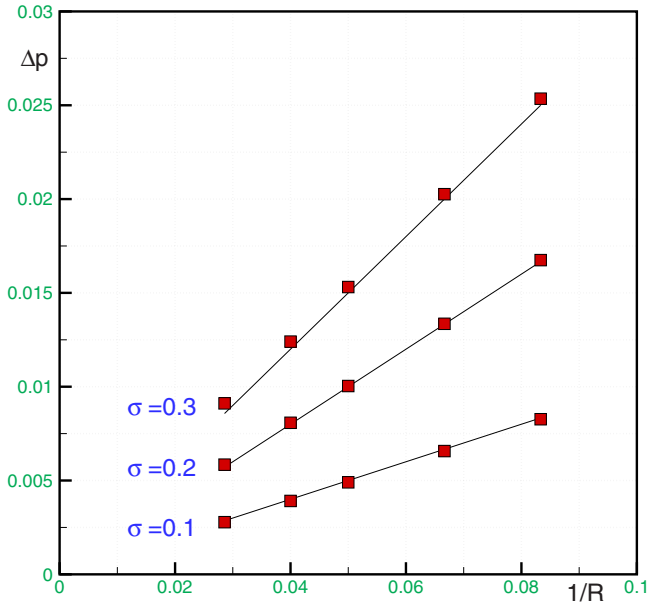

FIG. 1. (Color online) Verification of Laplace law for three different values for the surface tension ($\tau_f=\tau_g=0.503$, $\Gamma=100$, $W=5$).

In order to verify the Laplace law, stationary bubbles with different radii are generated inside the domain with 151 $\times$151 lattice points and periodic BC. The parameters are fixed at $\tau_f=\tau_g=0.503$, $\Gamma=100$, and $W=5$. Following the paper of Hou *et al.* [50], the pressure difference is measured by averaging the pressures inside and outside the bubble at lattice points away from $R\pm W$ after 50 000 iterations. The results are shown in Fig. 1 for three different values of surface-tension coefficient. It is seen that the MRT results are in good agreement with the theoretical solutions plotted by solid lines.

Figure 2 depicts the order-parameter profile as a function of the radial distance from the center of the bubble normalized by the bubble radius. As it can be seen, the numerical results of the present MRT model agree well with the analytical solution given by Eq. (8).

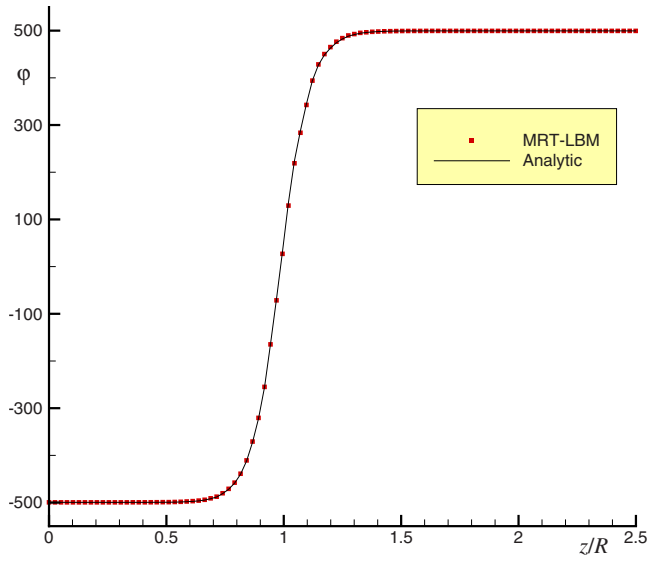

FIG. 2. (Color online) The order-parameter profile along the interface of a stationary fluid (bubble or drop).

TABLE I. The oscillating frequency of a capillary wave ($\nu=0.003$, $\Gamma=0.001$, $W=5$).

σ	ω (Theory)	ω (MRT-LBM)
0.002	0.913×10^{-3}	0.835×10^{-3}
0.004	1.305×10^{-3}	1.191×10^{-3}
0.005	1.463×10^{-3}	1.335×10^{-3}
0.006	1.613×10^{-3}	1.465×10^{-3}
0.008	1.607×10^{-3}	1.696×10^{-3}

B. Capillary wave

Another benchmark problem, which has been used extensively to assess the validity and accuracy of the diffuse interface methods [4,5], is the capillary-wave test. Chandrasekhar [51] gave an analytical solution for the case of two separated fluids with the same kinematic viscosity. In the long-wavelength limit, the decay rate and the oscillating frequency of an initially disturbed interface in the form of a sinusoidal perturbation could be calculated by taking, respectively, the real and imaginary parts of the following relation:

$$n=k_w^2\nu(y^2-1), \tag{34}$$

where k_w is the wave number and y is the physically meaningful roots of the following equation:

$$y^4+4\alpha y^3+2(1-6\alpha)y^2-4(1-3\alpha)y+1-4\alpha+s=0, \tag{35}$$

in which

$$\alpha=\frac{\rho_G\rho_L}{(\rho_G+\rho_L)^2},\quad s=\frac{\sigma}{k_w(\rho_G+\rho_L)\nu^2}. \tag{36}$$

Note that ρ_G and ρ_L are the densities of gas and liquid phases, respectively.

In order to satisfy the constraint of long-wavelength limit, a sinusoidal wave with amplitude of $0.05H$ (H being the height of the domain) is introduced to the order-parameter profile along the flat interface. The simulations are carried out in a lattice with 64×64 grid cells and the oscillating frequency of the capillary wave is evaluated for five values of surface tension, as given in Table I. The other parameters are $\tau_f=\tau_g=0.509$, $\Gamma=0.001$, and $W=5$. The BC in the horizontal direction is periodic while nonslip bounce-back BC is used in the vertical direction. As it is seen in Table I, the results are in the acceptable level of accuracy, compared to the theoretical solutions.

C. Wobbling bubble

As a fundamental subject of bubble dynamics [52,53], many researchers have investigated the problem of rising bubble under buoyancy using different multiphase LBMs

[28,54–56]. The important dimensionless parameters contributing to the motion of a bubble under gravity are Eötvös number, Morton number, and Reynolds number [52,53]

$$\mathrm{Eo} = \frac{g\Delta\rho D^2}{\sigma},$$

$$\mathrm{Mo} = \frac{g\Delta\rho\rho_L^2\nu_L^4}{\sigma^3},$$

$$\mathrm{Re} = \frac{u_t D}{\nu_L}, \tag{37}$$

where g is the magnitude of gravitational acceleration, $\Delta\rho$ is the density difference, D is the bubble diameter, ν_L is the kinematic viscosity of the liquid phase, and u_t is the terminal velocity of the rising bubble. The dimensionless time is also defined by

$$t^* = T\sqrt{\frac{g}{D}}, \tag{38}$$

where T is the number of iterations.

Hereafter, we postulate the Boussinesq approximation for binary fluids. According to the Boussinesq approximation, variation of the density is neglected except in the body force term. Thus, the body force is added to the bubble territory in the following manner:

$$\mathbf{F}_b = -\mathbf{g}\Delta n, \quad \text{where} \quad \varphi < 0, \tag{39}$$

in which Δn is the number density difference and the gravitational acceleration is pointing downward.

As an interesting application, the wake instability of a rising bubble at a low Morton value and high Reynolds number is simulated and the results are illustrated in Fig. 3. This problem has been observed, experimentally, by Tsuchiya and Fan [57]. Here, the computations are performed in a lattice with 121×241 points with the bounce-back BC at the surrounding walls. First, a bubble with $R=20$ and $\nu=0.003$ is placed at (60,40). The other parameters are $\tau_f=0.503$, $W=3$, and $\Gamma=0.4$. The corresponding Eötvös and Morton numbers are 16 and 9.8×10^{-7}, respectively. Figure 3 shows the flow pattern around the bubble at different times. As it is seen, at $t^*=11$, the flow field is symmetric and there exists a pair of vortices in the external flow. As time goes on, we can see two pairs of distinct vortices outside the bubble in Fig. 3(b). With further progress in time to $t^*=27$, the external flow clearly becomes asymmetric. In Fig. 3(d), the relevant Reynolds number is high enough to induce even a pair of small vortices in the bottom of the channel. Moreover, a pair of relatively big and asymmetric vortices is generated in the middle of the domain at $t^*=29$. The left vortex itself has two additional small circulations in it, while the right one is more uniform. It is worth noting that this wobbling pattern with its low Morton value may not be simulated with an LBGK model. This fact exhibits the superiority of the MRT-LBE to its LBGK counterpart.

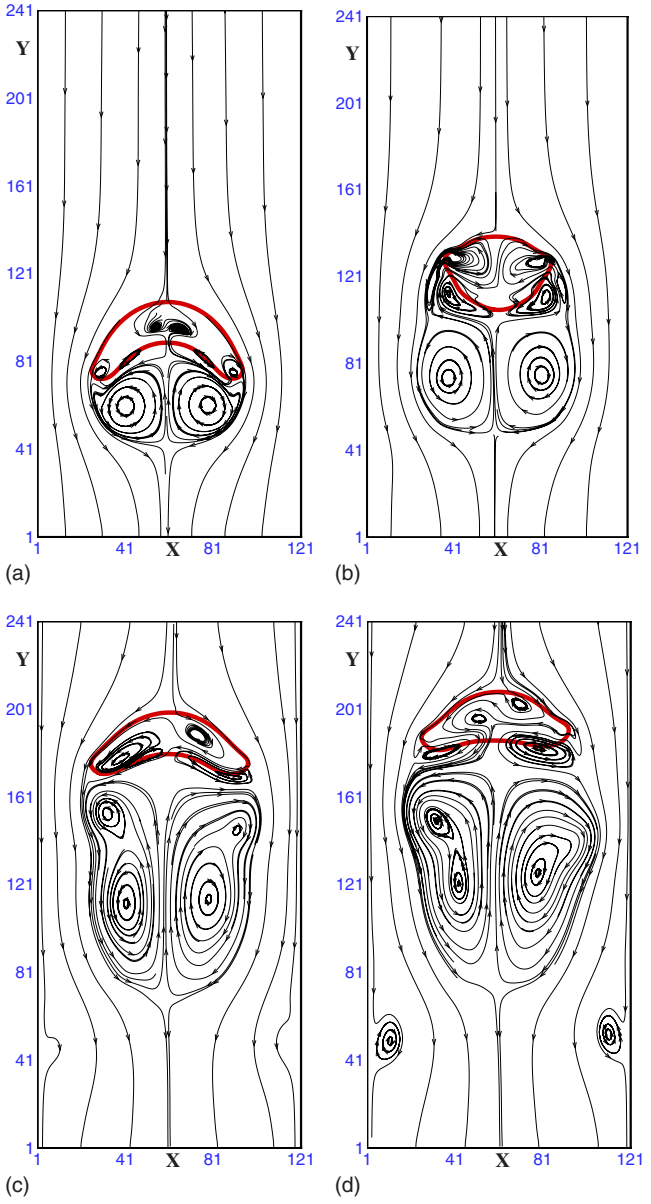

FIG. 3. (Color online) Streamlines around the wobbling bubble at a low Morton number (Eo=16, Mo=9.8×10^{-7}). (a) $t^*=11$; (b) $t^*=17$; (c) $t^*=27$; (d) $t^*=29$.

D. Turbulent flow

To shed more light on the supremacy of the present MRT-LBM over its BGK counterpart, another simulation in the same geometry is performed and the typical achievable viscosity values in the BGK and MRT models are compared to each other. In the first case, the relaxation time is $\tau_g=0.8$, which results in a viscosity value of $\nu=0.1$ and Mo=1.2×10^{-2}; while in the second case the relaxation parameter is $\tau_g=0.503$ which results in $\nu=0.001$ and Mo=1.2×10^{-10}. We can see that the viscosity value in the MRT model is 2 orders of magnitude smaller than that in the LBGK. The great advantage of reaching such a low viscosity value is clearly illustrated in Fig. 4. It is observed that while the flow pattern in Fig. 4(a) is laminar and symmetric, the flow field in Fig. 4(b) is absolutely asymmetric. Furthermore, some wiggles

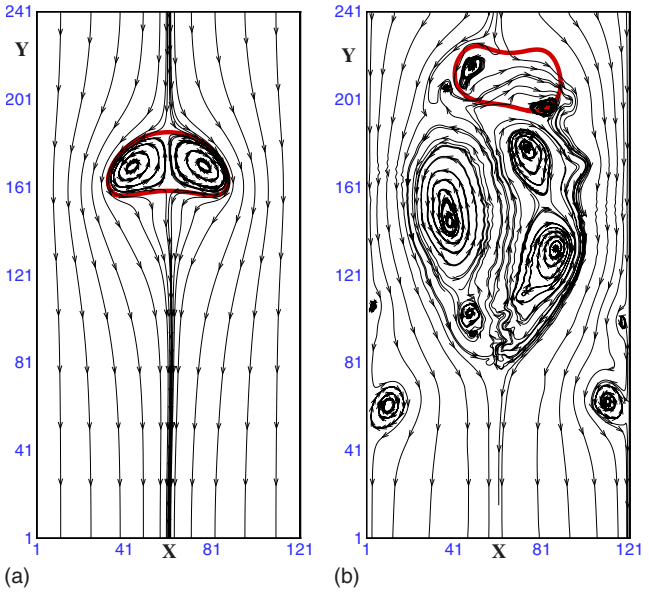

FIG. 4. (Color online) Rising bubble in a duct: comparison between (a) LBGK and (b) MRT-LBM results (Eo=16 and $t^*=34$). (a) $\tau_f=0.8$, $\tau_g=0.8$ (Mo=1.2×10^{-2}); (b) $\tau_f=0.501$, $\tau_g=0.503$ (Mo=1.2×10^{-10}).

are noticed in the wake of the violated wobbling bubble (compare to the streamlines in Fig. 3). The flow behind the bubble is most likely turbulent now, which is captured automatically by the MRT-LBM. It is worth mentioning that the LBM can be used as a direct numerical simulation (DNS) [6,55].

Variations of the Reynolds number for the wobbling bubble in a turbulent regime is plotted against the dimensionless time in Fig. 5 for two different BCs at the upper boundary. In the first run, the popular bounce back is applied at top, while in the second run the incoming distribution functions

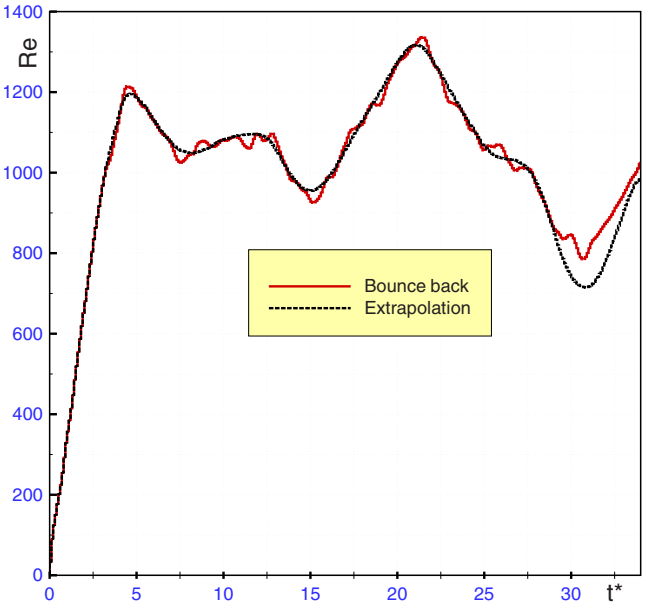

FIG. 5. (Color online) Variations of Reynolds number vs time for the wobbling bubble with Eo=16 and Mo=1.2×10^{-10}.

are extrapolated from their internal values [58]. This may be interpreted as the absorbing BC [59] with the second order of accuracy. It is seen that the extrapolating scheme effectively reduces the fluctuations in the rise velocity. In fact, the pressure waves reflecting from the top wall are the reason of these oscillations for the bounce-back BC. Thus, the extrapolation BC justifies calling it absorbing BC [59].

E. Moving droplet

As we mentioned before, physically, the model of Zheng *et al.* [35] is unable to simulate multiphase flow with any noticeable density difference. Here, using the numerical scheme, we will show that the method in [35] is actually a density-matched binary-fluid model. To prove this claim numerically, two sets of simulations are conducted.

First, we compare the model in [35] to the kinetic-based LBM [23,56], which is a well-established method specifically powerful in investigation of droplet dynamics [24–26]. Hence, we examine the evolution of a droplet that is injected suddenly into a quiescent gas phase. Since the density in the kinetic-based LBM is the real density of the fluid, it permits us to inspect the effect of density ratio on the flow pattern and, in particular, on the interval of which the drop moves. In other words, it is expected that the droplet with a higher density travels more distance relative to the less dense droplet.

In order to manifest the impact of density ratio, a droplet is placed in a computational domain with 181×61 lattice cells. Free-slip BCs are applied at all boundaries, with special treatment of the symmetric boundary at $y=0$. Initial radius of the drop is 15 and it is placed 31 lattice units away from the left wall. The common parameters are $\tau_f=\tau_g=0.8$, $\sigma=0.002$, and $W=2$ and the initial relative velocity $U_0=0.1$. The mobility in the free-energy model is fixed at $\Gamma=0.3$. Figure 6 depicts the evolution of the droplet with two different density ratios at the same time. The results of the kinetic-based MRT-LBM [56] are shown on top, while the bottom part of Fig. 6 is related to the binary-fluid model. In Fig. 6(a), the densities are chosen such that the Boussinesq approximation holds; i.e., $\rho_G=1$ and $\rho_L=1.2$ for the kinetic-based LBM, which corresponds to $n_A=1$ and $n_B=1.2$ in the free-energy model. To illustrate the point, the density of the drop in Fig. 6(b) is increased to $\rho_L=10$ ($n_B=10$). In Fig. 6(a), the free-energy model coincides with the kinetic-based model more or less. This agreement is due to the postulation of the Boussinesq approximation in selection of the densities. Nevertheless, in Fig. 6(b), a major discrepancy is apparent. As a matter of fact, here the density and, hence, the momentum of the droplet are higher than previous case; therefore, as it was expected, the drop in the kinetic-based model travels more distance. But, in contrary to the kinetic-based method, the drop in the free-energy-based LBM does not move as much distant as its kinetic-based counterpart. This is because of the fact that neither the density of the drop nor that of the ambient fluid is accounted for directly in the relevant equations of the former model. Strictly speaking, it is not clear at all whether the assumed droplet in the free-energy-based method is heavy phase (drop) or light phase (bubble).

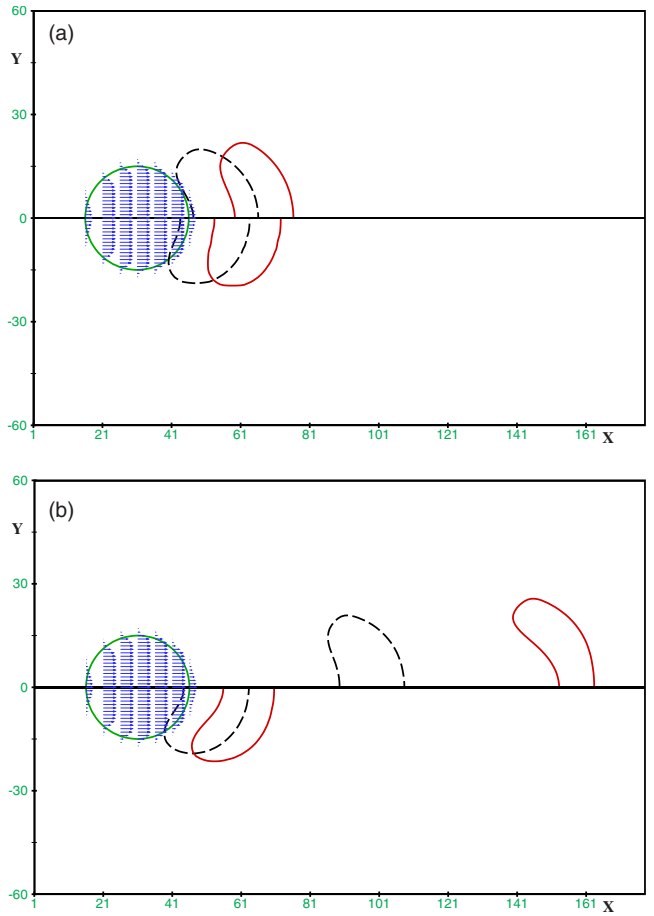

FIG. 6. (Color online) Effect of number densities on the flow pattern around a moving drop with $\rho_G=n_A=1$; comparison of the kinetic-based LBM [26] (top) with the binary-fluid model [35] (bottom). (a) $\rho_L=n_B=1.2$; (b) $\rho_L=n_B=10$.

It might be concluded that the number densities that simultaneously satisfy Eqs. (3) and (5) are unique. However, it should be pointed that the role of parameter φ is just to track the interface between different phases and it has no any contribution to the hydrodynamic equations. In other words, the order parameter can assume any arbitrary value without loss of generality; of course, the mobility should be manipulated to avoid numerical instability. For instance, φ^* was chosen to be to unity in Ref. [48]. To resolve this misleading issue, another test is carried out and the results are shown in Fig. 7. The nominal densities are $n_A=1$ and $n_B=1000$ for the first case and $n_A=500$ and $n_B=501$ for the second case. Note that both situations have an average number density equal to 500.5; albeit, the seductive density ratio in the first case seems to be 1000. However, the density ratio is not definable here, i.e., the model is suitable for a density-matched binary fluid, because, as it is seen in Fig. 7, the results of both cases match exactly.

IV. MRT-LBM FOR MULTIPHASE FLOWS WITH A DENSITY CONTRAST

As it was shown in the previous section, the free-energy-based models [20,35] are not capable of dealing with two-

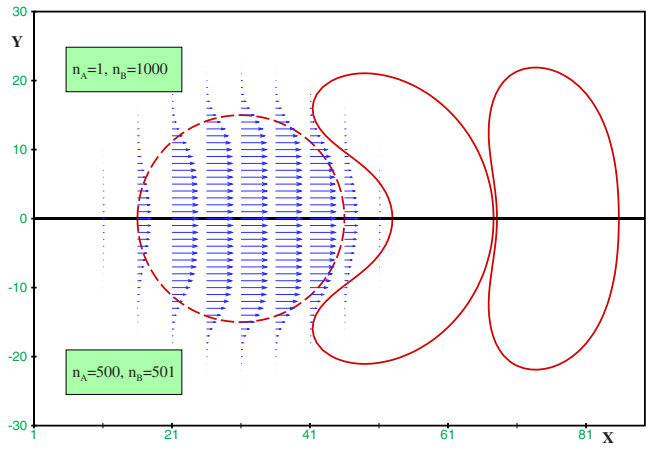

FIG. 7. (Color online) Flow pattern around a moving drop for different number densities with the same average density ($n=500.5$). Top: $n_A=1$, $n_B=1000$, $\Gamma=1000$; bottom: $n_A=500$, $n_B=501$, $\Gamma=0.001$.

phase flows with different densities and are mostly suitable for the binary fluids in which the Boussinesq approximation holds. In fact, most of the existing diffuse models are restricted to the density-matched fluids [47–49]. This fact motivates us to propose an LBE for multiphase flows based on the phase-field modeling that can be used for a more realistic situation of two fluids with a density contrast. We start with the NSE for multiphase flows, which may be written as

$$\frac{\partial \rho \mathbf{u}}{\partial t} + \nabla \cdot (\rho \mathbf{u}\mathbf{u}) = -\nabla \cdot \mathbf{P} + \nabla \cdot \Pi + \mathbf{F}_b, \tag{40}$$

where $\mathbf{\Pi}=\mu(\nabla \mathbf{u}+\mathbf{u}\nabla)$ is the viscous stress tensor. Using the thermodynamic identity [47]

$$\nabla \cdot \mathbf{P} = \varphi \nabla \mu_\varphi + \nabla S_p \tag{41}$$

together with the following relation:

$$\nabla(\varphi \mu_\varphi) = \varphi \nabla \mu_\varphi + \mu_\varphi \nabla \varphi, \tag{42}$$

we arrive at the following NSE:

$$\frac{\partial \rho \mathbf{u}}{\partial t} + \nabla \cdot (\rho \mathbf{u}\mathbf{u}) = -\nabla p + \nabla \cdot \Pi + \mathbf{F}_s + \mathbf{F}_b, \tag{43}$$

in which the surface-tension force was defined in Eq. (24) and the pressure assumes the following form now:

$$p = S_p + \varphi \mu_\varphi. \tag{44}$$

Note that S_p is used to enforce incompressibility [47,49]. In Refs. [35,48,49], $S_p=nc_s^2$ was used, but we leave it intact and update the pressure by solving a pressure evolution equation in the framework of the LBM. Also, as regard to the existence of Laplacian operator in the definition of chemical potential [Eq. (9)] from the numerical perspective, it is better to use the potential form of the surface tension [33].

Here, the interface-capturing equation evolves according to Eq. (11) with the popular BGK collision model. However, to obtain the hydrodynamic equations, we start from the Boltzmann equation for nonideal fluids [22]

$$\frac{Dh}{Dt} = \frac{\partial h}{\partial t} + \xi \cdot \nabla h = -\mathbf{S}(h - h^{eq}) + \frac{(\xi - \mathbf{u}) \cdot (\mathbf{F}_s + \mathbf{F}_b)}{\rho RT} h^{eq}, \tag{45}$$

where h is the conventional particle distribution function, ξ is the microscopic velocity, and h^{eq} is the usual equilibrium distribution function in velocity space. The equilibrium distribution function should be constructed in such a way that the Chapman-Enskog expansion leads to the macroscopic NSE in Eq. (43). Hence, the following variable is introduced first [23]:

$$g = hRT + (p - \rho RT)\frac{h(\mathbf{0})}{\rho}. \tag{46}$$

After substitution of Eq. (46) into the Boltzmann equation and assuming proper incompressibility approximations [23,32], one can easily find

$$\frac{Dg}{Dt} = -\mathbf{S}(g - g^{eq}) + \frac{(\xi - \mathbf{u})}{\rho} \cdot \{h^{eq}(\mathbf{F}_s + \mathbf{F}_b) + [h^{eq} - h^{eq}(\mathbf{0})]\nabla(\rho RT)\}. \tag{47}$$

As we are interested in incompressible limit that the Mach number is small, $\mathrm{Ma} < 1$, the term ∇p, which is of $O(\mathrm{Ma}^2)$ multiplied by $[h^{eq} - h^{eq}(\mathbf{0})]$ of $O(\mathrm{Ma})$, is dropped from Eq. (47) [32]. Now that Eq. (47) must be integrated to be solved, the trapezoidal rule shall be used [22]. Hence, the following transformation variable is utilized to get an explicit method [22,23]:

$$\bar{g} = g - \frac{1}{2}F^g, \tag{48}$$

where

$$F^g = \frac{(\xi - \mathbf{u})}{\rho} \cdot \{h^{eq}(\mathbf{F}_s + \mathbf{F}_b) + [h^{eq} - h^{eq}(\mathbf{0})]\nabla(\rho RT)\}\delta_t. \tag{49}$$

After discretization of velocity space in a D2Q9 lattice, it is straightforward to show that the evolution equation for modified pressure distribution function reads as

$$\bar{g}_\alpha(\mathbf{x} + \mathbf{e}_\alpha \delta_t, t + \delta_t) = \bar{g}_\alpha(\mathbf{x}, t) - S_{\alpha i}(\bar{g}_i - g_i^{eq}) + F_\alpha^g - \frac{1}{2}S_{\alpha i}F_i^g, \tag{50}$$

in which

$$g_\alpha^{eq} = w_\alpha \left[p + \rho RT\left(3\mathbf{e}_\alpha \cdot \mathbf{u} + \frac{9}{2}(\mathbf{e}_\alpha \cdot \mathbf{u})^2 - \frac{3}{2}u^2\right)\right]. \tag{51}$$

The Chapman-Enskog multiscale analysis shows that the above constraints lead to the NSE in Eq. (43) with the second order of accuracy. After multiplying Eq. (50) by the transformation matrix, the discretized equation in moment space obtains as

$$\hat{g}_\alpha(\mathbf{x} + \mathbf{e}_\alpha \delta_t, t + \delta_t) = \hat{g}_\alpha(\mathbf{x}, t) - \hat{S}_{\alpha i}(\hat{g}_i - \hat{g}_i^{eq}) + \hat{F}_\alpha^g - \frac{1}{2}\hat{S}_{\alpha i}\hat{F}_i^g, \tag{52}$$

where

$$\hat{g}_\alpha = M_{\alpha i}\bar{g}_i; \quad \hat{g}_\alpha^{eq} = M_{\alpha i}g_i^{eq}; \quad \hat{F}_\alpha^g = M_{\alpha i}F_i^g. \tag{53}$$

The macroscopic properties are calculated by

$$\rho = \rho_G + \frac{\varphi + \varphi^*}{2\varphi^*}(\rho_L - \rho_G), \tag{54}$$

$$p = \sum_{\alpha=0}^{8} \bar{g}_\alpha + \frac{\delta_t}{2}\mathbf{u} \cdot \nabla(\rho RT), \tag{55}$$

$$\rho RT\mathbf{u} = \sum_{\alpha=1}^{8} \bar{g}_\alpha \mathbf{e}_\alpha + \frac{\delta_t}{2}(\mathbf{F}_s + \mathbf{F}_b). \tag{56}$$

It should be mentioned that there are two major differences between the proposed method in this section and the free–energy-based model [20,35]. First, instead of the average density, the real density of the fluid is incorporated in the equilibrium distribution function [Eq. (51)] by using Eq. (54). Second, and more importantly, in the present scheme, the pressure of the fluid is updated correctly using a pressure evolution routine in Eq. (55). This is in contrast to the free-energy approach [35] in which the pressure was assumed constant and equal to the ideal-gas pressure. On the other hand, the basic difference between the proposed model and the kinetic-based model lies in the nature of the interface tracking equations. In fact, in the kinetic-based LBM, the interface tracking equation is based on the equation of state, by which the intermolecular forces cause different phases to be separated. As a result, the Cahn-Hilliard equation recovers with additional pressure-related terms [23,35], while a proper chemical potential μ_ϕ which is related to a free-energy functional is used in the phase-field model. Consequently, the Cahn-Hilliard equation recovers without any additional terms up to the second order of accuracy [46]. Furthermore, in the kinetic-based model, the minimum and maximum values of the index function should be evaluated either via the two-layer fluid problem or by using Maxwell's equal area construction [23,42]. However, these values can be arbitrarily chosen in the current model. Moreover, the forcing terms in the above-mentioned models are slightly different although the origin of the evolution equation for hydrodynamic properties, namely, pressure and velocity, for both models are similar. There are some other minor differences as well. For instance, the surface tension in the kinetic-based model is not known *a priori* and should be evaluated from the two-layer simulation, but it is known in advance in the phase-field modeling.

V. RESULTS FOR THE PHASE-FIELD MRT-LBM

Now, the proposed LBM will be examined for accuracy and stability at low viscosities. Henceforth, the order-parameter distribution function f_α is relaxed to its equilibrium value; in other words $\tau_f = 1$.

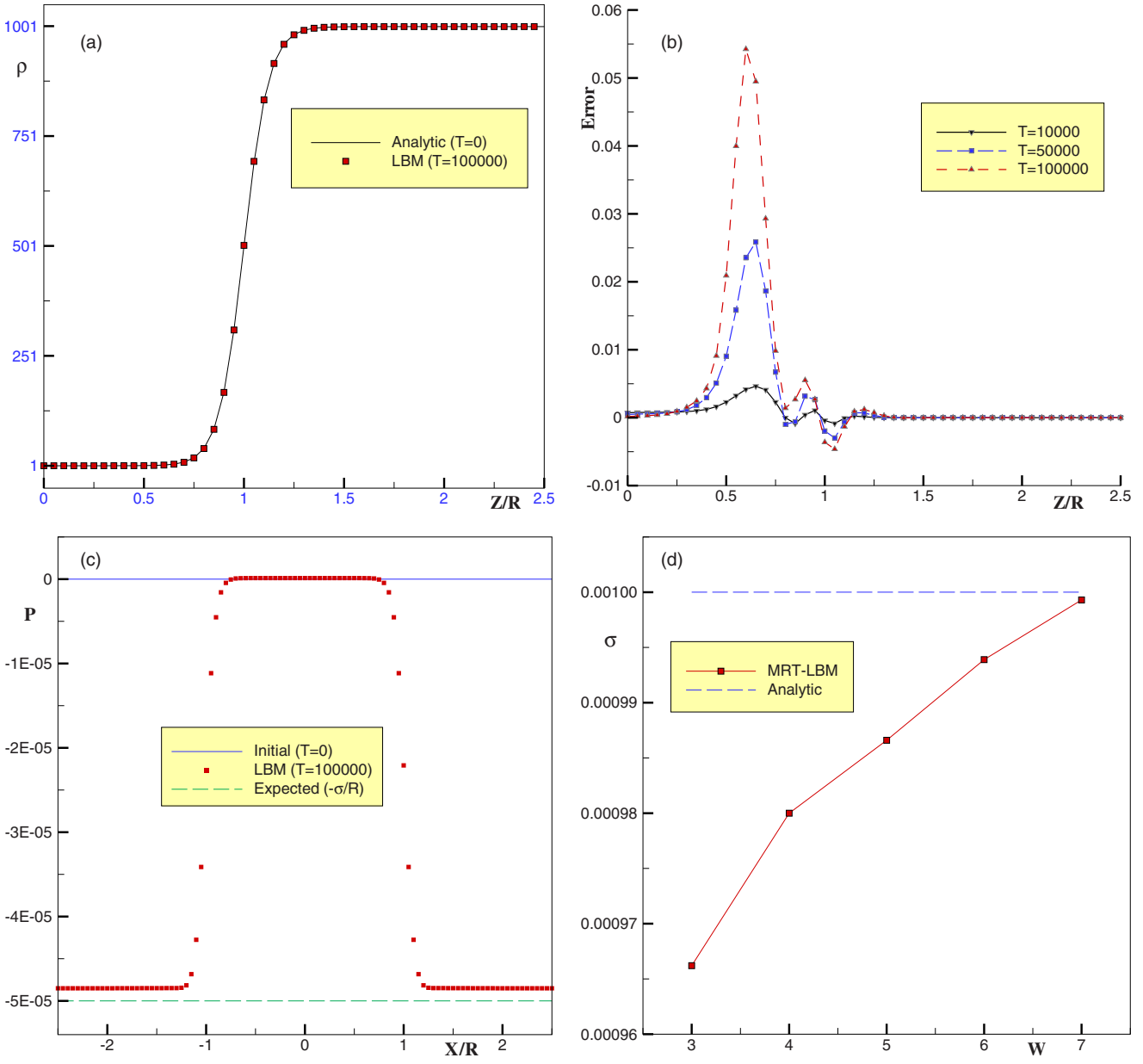

FIG. 8. (Color online) Density and pressure profiles around the interface of a stationary bubble ($\rho_G=1$, $\rho_L=1000$, $\nu=0.01$). (a) Density profile; (b) diffusion error; (c) pressure distribution; (d) effect on the interface width.

A. Stationary bubble test

First, we place a circular bubble in the middle of a domain with 101×101 lattice cells and periodic BC. The parameters are $\rho_G=1$, $\rho_L=1000$, $\nu=0.01$, $\Gamma=0.01$, $\sigma=0.001$, and $W=5$. At the beginning, the initial pressure of the whole fluid is set to zero. If the pressure is updated correctly, it is expected that, after a long time, the density profile remains unchanged and the pressure jump across the interface fulfills the Laplace law. Figure 8(a) shows the density profile as a function of the radial distance from the center of the bubble normalized by its radius. As it is seen, even after 100 000 iterations, the bubble retains its original shape and the density profile matches the analytical solution, which is representative of the hyperbolic profile for the bubble configuration at $T=0$. The relative error of the evaluated density profile, defined by the discrepancy between the numerical and analytical densities divided by the analytical solution, is plotted in Fig. 8(b). As it is seen, after 100 000 iterations, the maximum dimensionless error, which occurred near the interface in the bubble region, is less than 6%. However, we notice that the relative error increases with time. In the simulations, we found that there is a strong dependence between the diffusion of the light phase into the heavy phase and the mobility. This issue will be discussed later. Moreover, as demonstrated in Fig. 8(c), the pressure distribution around the bubble is modified to align with the expected pressure jump across the interface, according to Eq. (29). The minor discrepancy between the predicted pressure outside the bubble and the anticipated value is due to the finite thickness of the interface. It is expected that increase of the interface width would re-

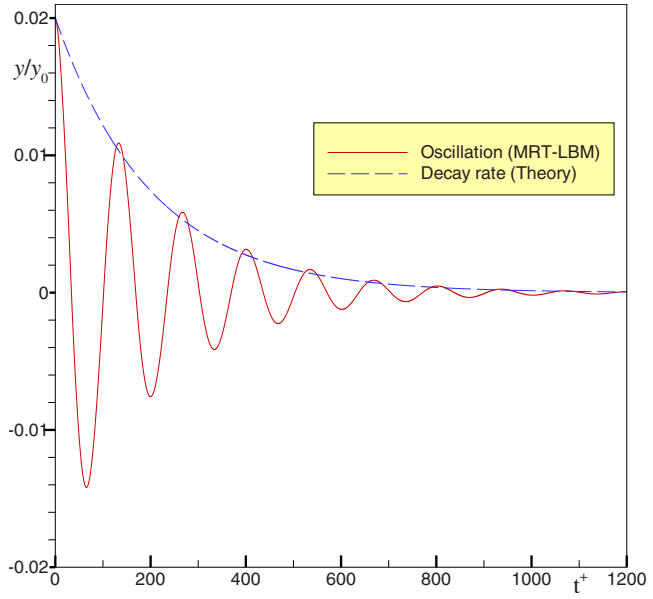

FIG. 9. (Color online) Oscillations and dissipation of a capillary wave ($\rho_G=1$, $\rho_L=100$, $\nu=0.003$).

sult in more accurate answers as revealed in Fig. 8(d). We can see that by increasing the interfacial thickness, the numerical results approach the actual value, similar to previous studies [32,35].

B. Capillary wave

As another benchmark, a sinusoidal density profile with an amplitude of $0.02H$ is established along a flat interface in a domain with $N_x=N_y=64$. The other parameters are $\rho_G=1$, $\rho_L=100$, $\nu=0.003$, $\Gamma=2$, $\sigma=0.03$, and $W=5$. The oscillation frequency of the capillary wave, as well as the analytical decay rate given by Eq. (34), is calculated and the results are shown in Fig. 9. In this figure, the horizontal axis is the dimensionless time defined by

$$t^+ = \frac{T\sigma k_w}{\nu(\rho_G+\rho_L)}. \tag{57}$$

As it is seen, the general behavior of decay rate of the capillary wave obeys the theoretical prediction; however, there can be notice some small overestimates in oscillations. In fact, the oscillation and decay rate of the capillary wave depend on both the interface width and mobility. Examination of the influence of these parameters and the impact of relaxation time τ_f is not in the scope of the present study and needs further investigations.

Although the stationary bubble and capillary-wave tests with high-density ratios were conducted successfully, they were the static cases in which the velocity had not came into play significantly. Strictly speaking, as the velocity increases, the maximum achievable density ratio in the model decreases. We suspect two reasons for this issue. First and most likely, the bulk free-energy density given by Eq. (4) may not be a good selection for a high-density ratio fluid which undergoes a rapid velocity change. As a matter of fact, this form of free energy is the simplification of the van der Waals EOS at equilibrium [32,33]. Therefore, it is reasonable to seek for another free-energy density function that more accurately specifies the state of the fluids far from equilibrium. Second, as the velocity increases, the compressibility errors become significant which, in turn, results in the violation of low Mach number approximation and, therefore, instability. Since the focus of the current study is on the development of a phase-field model in the context of the MRT-LBM, we shall restrict ourselves to moderate density ratios but low viscosity values.

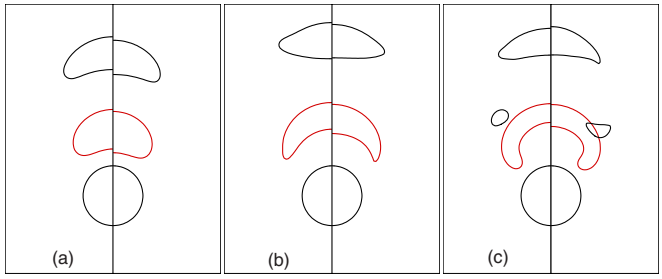

FIG. 10. (Color online) Rising bubble: comparison of the phase-field MRT-LBM (right) to its kinetic-based counterpart (left) $t^*=0,3,6$ ($\rho_G=1$, $\rho_L=5$). (a) Eo=21.6, Mo=1.5×10^{-1}; (b) Eo=21.6, Mo=1.5×10^{-5}; (c) Eo=86.4, Mo=9.6×10^{-4}.

C. Buoyancy driven motion of a bubble at low Morton numbers

It is a good practice to compare the current model to other existing LBMs. Hence, at first, the present phase-field MRT-LBM is compared to its kinetic-based counterpart [56]. For both of the models, a circular bubble with an interfacial thickness of three cells is located 41 units above the bottom boundary in a domain with 101×201 lattice points. Due to the symmetry with respect to the vertical axis, computations are carried out only in a half of the channel. The bounce-back BC is applied at the surrounding walls except for the axis of symmetry where the special reflection BC is used. In contrary to the MRT-LBM for binary mixtures described in Sec. II, now the gravitational effects can be applied to the entire fluid by incorporating the following body force term everywhere:

$$\mathbf{F}_b = (\rho-\rho_L)\mathbf{g}. \tag{58}$$

It is obvious that the above forcing term leads to the net buoyancy force of $(\rho_G-\rho_L)\mathbf{g}$ in the gas phase and vanishes in the liquid phase.

The results shown in Fig. 10 are for a rising bubble with $R=15$, $\rho_G=1$, and $\rho_L=5$, with different Eötvös and Morton numbers. Although the bubble shapes are rather similar for all the patterns in both the models, we notice that the rise velocity of the phase-field LBM is slightly smaller than the kinetic-based model. Moreover, we see that both of the evaluated methods predict the skirt breakup of the bubble at Eo=86.4 and Mo=9.6×10^{-4} in Fig. 10(c) (different breakup modes of a rising bubble are studied in more detail in Ref. [56]). It is worth noting that most of the sharp interface methods [4,5] fail to deal with fast topological changes such

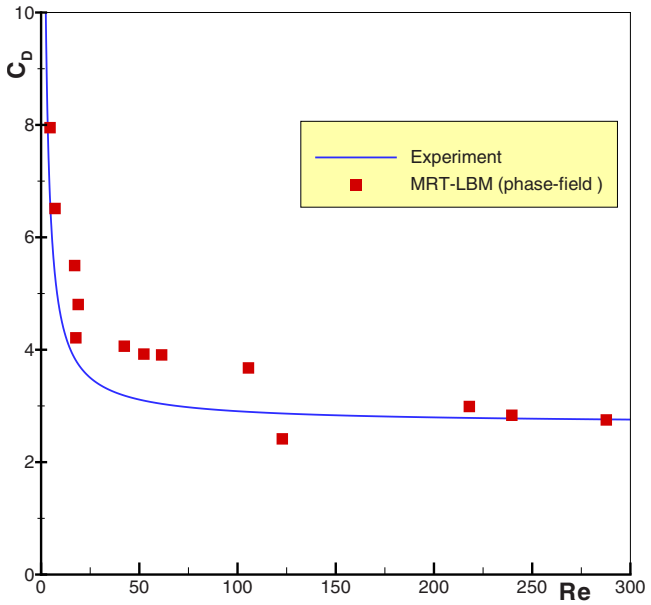

FIG. 11. (Color online) Drag coefficient of a cylindrical bubble vs Reynolds number.

as breakup and coalescence. This reveals the superiority and popularity of the diffuse interface models, especially LBM, over the conventional sharp interface schemes.

Now, we report on the case of bubble rising due to gravity at extremely low Morton numbers (low viscosity values). Thanks to the symmetry with regard to the vertical axis, computations are carried out only in the right half of the domain. Should the boundary effects be neglected, the width of the channel must be larger than 10 times the bubble radius [52,53]. Therefore, we pick a computational lattice with size of 200×300. The BCs at right, bottom, and top walls are bounce back, while symmetric BC is used at the left boundary. The numerical parameters are $\rho_G=1$, $\rho_L=3$, $R=20$, $\Gamma=0.1$, and $W=3$. The relevant Morton number ranges from 1.6 to 4.3×10^{-8}. Initially, the bubble is located at (1,41). After the bubble reaches a steady shape, its drag coefficient can be found from the balance between the buoyancy and drag forces. For a cylindrical bubble, we have

$$C_D=\frac{\pi g}{u_t^2}\frac{\Delta\rho}{\rho_L}\frac{R^2}{R_C}, \tag{59}$$

in which R_c is the cross-stream radius of the 2D bubble.

The drag coefficient of the bubble rising at low Morton values is plotted against the Reynolds number in Fig. 11. The solid line shows the empirical correlation given by [53]

$$C_D^{\text{exp}}=\left[(2.67)^{0.9}+\left(\frac{16}{\text{Re}}\right)^{0.9}\right]^{1/0.9}. \tag{60}$$

As it is seen in Fig. 11, at moderate Reynolds numbers, the MRT results overestimate the drag coefficient compared to the experimental data. The main reason of this discrepancy is that our simulations are in two dimensions while the empirical correlation is for 3D bubbles. On the other hand, the terminal velocity of the bubbles at higher Reynolds numbers is nearly constant. This is in line with experimental observations which showed that the rise velocity of a bubble at low Morton values is independent of the other parameters and, hence, the corresponding drag coefficient remains approximately unchanged at high Reynolds numbers.

D. Droplet splash on a wet surface

In order to assess the accuracy of the proposed model, droplet splash on a wet surface is simulated and the spread radius is measured for three different Reynolds numbers. This phenomenon happens in many industrial applications such as print sprays and combustion engines, as well as in natural processes such as raindrops. As it is mentioned in other studies [32,43,60], dimensional analysis suggests two major nondimensional numbers, namely, Reynolds and Weber numbers

$$\text{Re}=\frac{U_0D}{\nu_L},$$

$$\text{We}=\frac{\rho_LU_0^2D}{\sigma}, \tag{61}$$

where U_0 is the velocity of the drop at the instant of impact on the wet surface. According to the potential flow solution [60], the spread radius of the droplet as a function of the short time after splash is of the form

$$r=\sqrt{DU_0T}. \tag{62}$$

Also, the dimensionless time is defined as

$$t^*=\frac{TU_0}{D}. \tag{63}$$

In the simulation of a droplet splash, a computational domain with 600×400 lattice cells is used. Left boundary is the axis of symmetry, while bounce-back BC is invoked at the bottom wall and free-slip BC is utilized at top. The right boundary is open and extrapolation is used to determine the incoming distribution functions. The simulation parameters are $R=100$, $\rho_G=1$, $\rho_L=5$, $U_0=0.05$, $\Gamma=90$, and the height of the wet surface is one-tenths of the entire domain height. The Weber number is fixed at We=5000, while the Reynolds number is changed from 50 to 1000 by tuning the viscosity. The qualitative results are shown in Fig. 12. In each frame, the results for the current phase-field MRT-LBM are shown on the right, while the findings of the kinetic-based model are mirrored on the left for comparison. It is seen that the outcomes of the kinetic-based LBM and phase-field approach are similar. Also noticed is the increase of deformation rates with the Reynolds number. The results for Re=50 in Fig. 12(a) shows more smooth deposition of the droplet on the wet surface, while increase of Reynolds number results in a more intensive splash. In particular, at final times in Fig. 12(c) for Re=1000, we notice some sort of Taylor instabilities.

The spread radius of the drop along with the theoretical solution [Eq. (62)] is shown in the log-log plot in Fig. 13. As it is observed, the evaluated spread radius is in accord with the linear prediction of potential flow [60], though, similar to

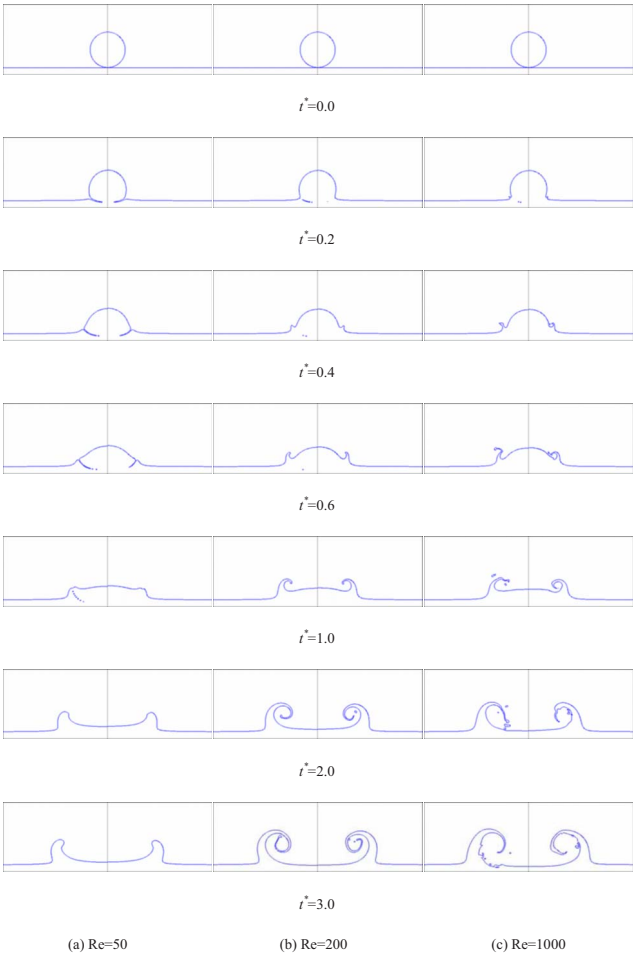

FIG. 12. (Color online) Droplet splashing on a wet surface. Left: Re=50; middle: Re=200; right: Re=1000. In each column, the left frames represent the kinetic-based LBM and the frames on the right are for the phase-field model.

previous works [32,43], the numerical results overestimate the analytical solution at initial times. Also, we see that the results of the kinetic-based LBM for Re=50 and 200 are slightly above those of the phase-field model.

E. Falling droplet

Finally, as another application of the multiphase flows, we chose to simulate the evolution of a falling droplet under gravity, which is of great importance in study of droplet dynamics. The results are presented for a typical *bag breakup* of the falling drop under buoyancy forces. The simulations are carried out in a lattice with 150×450 cells. Here, again, symmetry BC is utilized at the axis of symmetry and nonslip bounce-back BC is used elsewhere. The common parameters are $\rho_G=1$, $\rho_L=5$, and $\tau_g=0.7$. The relevant dimensionless numbers are Eo=21.6 and Ar=22.9, where the Archimedes number—also called the gravity Reynolds number—is defined below:

$$\mathrm{Ar}=\frac{\sqrt{gD^3}}{\nu_L}. \tag{64}$$

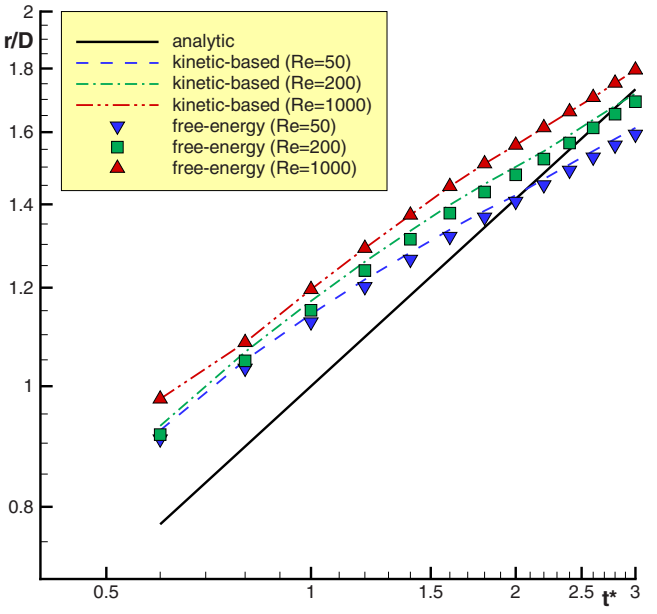

FIG. 13. (Color online) Spread radius of the droplet splashing on a wet surface.

Figure 14 depicts the evolution of the drop as it falls. As it is seen, the quality of the results of the present LBM is more or less akin to the kinetic-based findings [25] with some tiny discrepancies. At first, up to $t^*=5$, the droplet in the kinetic-based model supersedes the free-energy results. However, as time goes on, the kinetic-based drop gets more stretched in the radial direction relative to the free-energy drop. Consequently, its fall velocity reduces due to higher drag force exerted on the surface of the drop. This is evident

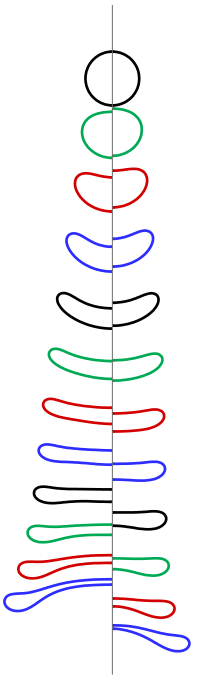

FIG. 14. (Color online) Deformation of a falling droplet with Eo=21.6 and Ar=22.9 ($t^*=0$ to 12); comparison between the kinetic-based model (left) and phase-field LBM (right).

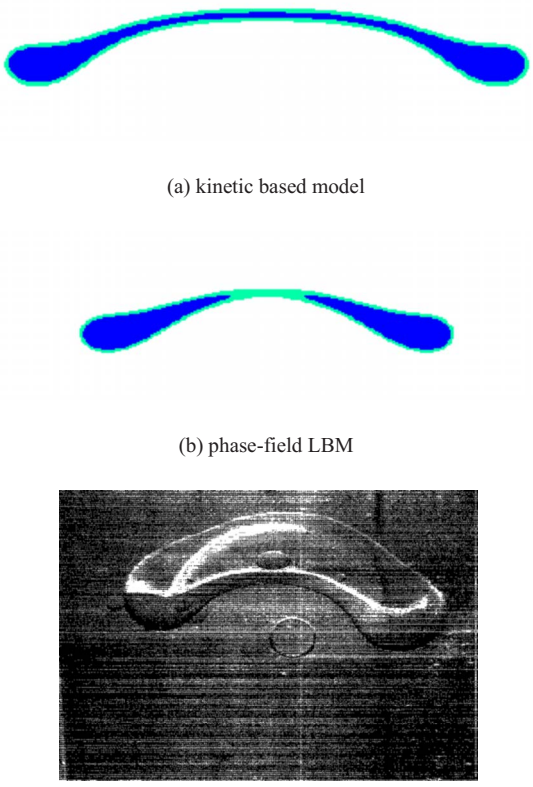

(a) kinetic based model

(b) phase-field LBM

(c) experimental observations

FIG. 15. (Color online) Onset of the bag breakup mechanism at $t^*=12$ (the last frame corresponds to Fig. 6 in Ref. [61]).

at $t^*=6-12$ in Fig. 14, where the droplet on the right frame surpasses the left drop. However, the droplet in both of the methods assumes a bag-type shape at $t^*=12$.

The final shape of the falling drops is illustrated in Fig. 15 together with the experimental evidence of the bag breakup mechanism [61]. Although the 2D simulations with both the free-energy and kinetic-based models predict the onset of bag breakup at $t^*=12$, the width of the bag is further for the kinetic-based LBM. This behavior also was noticed in the droplet splash on a wet surface in Fig. 13, where the spread radius for the kinetic-based model was a little more than that of the phase-field approach.

In sum, both of the models emerged as powerful and reliable numerical methods for handling various deformation and disintegration modes of the rising bubble and falling droplets—the representatives of bubble and droplet dynamics—and, in general, for simulation of multiphase flows. Both models are well suited for parallelization. Although both of the methods can be used to simulate fast topological changes and breakup, it was found that the proposed free-energy method is 1.3 times faster than the kinetic-based model. The kinetic-based method seems to be more stable than the free-energy-based model whenever the rate of interfacial deformation is higher. In fact, the presented model is very sensitive to the mobility value. Lower mobility reduces the diffusion for the cases where the velocity does not play an important role, hence increases the stability of the model, while progressively larger mobility is needed for stability of the model at higher rate changes and velocities. Nevertheless, further investigations are needed to claim the superiority of each model to the other in terms of accuracy and stability.

VI. SUMMARY AND CONCLUSION

In this paper, a multiple-relaxation-time lattice Boltzmann method for binary fluids was developed first. The proposed model can tolerate very low viscosity values and it proved to be a promising scheme for simulating immiscible multiphase flows at high Reynolds numbers. As an interesting application, the motion of a Boussinesq bubble under buoyancy effect was considered and the turbulent flow behind the wobbling bubble was observed.

Next, as a remedy for the free-energy models that are restricted to density-matched fluids, a multiphase MRT-LBM based on the phase-field modeling was proposed. The suggested LBM can easily deal with the situations where the rate of deformation is so high that may lead to the interface breakup. A variety of test studies were conducted and the results were compared to analytical and experimental data, as well as comparison to the kinetic-based LBM: the drag coefficient of the rising bubble was found to be in satisfactory agreement with empirical correlations, the spread factor of the droplet splash on a wet surface was in good accordance with the linear prediction of theoretical solution, and the quality of breakup of a falling droplet in the bag mode was in coincidence with experimental observation.

As it was declared before, the proposed model becomes unstable at high-density ratios whenever the velocity rate change is high. Examining the other forms for the bulk free-energy density in Eq. (4), as well as implementing a concentration- or velocity-dependent mobility in the convective Cahn-Hilliard equation, Eq. (1), should be contemplated in future studies. Also, extension of the models to 3D is straightforward [62,63]. These are the subjects of future works.

APPENDIX: DISTRIBUTION FUNCTIONS AND FORCING TERM IN MOMENT SPACE FOR THE DENSITY-MATCHED BINARY FLUID MODEL

The equilibrium distribution functions in moment space could be found by premultiplying the equilibrium distributions in velocity space by the transformation matrix [see Eq. (14)]. Thus, the equilibrium distribution functions in moment space read as

$$\hat{f}_\alpha^{eq}=\begin{bmatrix}\varphi\\ -4\varphi+6\mu_\varphi\Gamma\\ 4\varphi-9\mu_\varphi\Gamma\\ \varphi u_x\\ -\varphi u_x\\ \varphi u_y\\ -\varphi u_y\\ 0\\ 0\end{bmatrix}, \tag{A1}$$

$$\hat{g}_\alpha^{eq} = \begin{bmatrix} n \\ -2n + 3nu^2 + 6\varphi\mu_\varphi \\ n - 3nu^2 - 9\varphi\mu_\varphi \\ nu_x \\ -nu_x \\ nu_y \\ -nu_y \\ n(u_x^2 - u_y^2) \\ nu_x u_y \end{bmatrix}. \tag{A2}$$

As mentioned before, suitable coding techniques can effectively reduce the computational cost by avoiding matrix operations [41]. Hence, it is wise to calculate the forcing term in moment space beforehand and use that in the collision process. The forcing term [Eq. (23)] in moment space may be written as

$$\hat{F}_\alpha = M_{\alpha i} F_i = \begin{bmatrix} 0 \\ 6(\mathbf{u}\cdot\mathbf{F}) \\ -6(\mathbf{u}\cdot\mathbf{F}) \\ F_x \\ -F_x \\ F_y \\ -F_y \\ 2(u_x F_x - u_y F_y) \\ u_x F_y + u_y F_x \end{bmatrix}. \tag{A3}$$

[1] C. W. Hirt and B. D. Nichols, J. Comput. Phys. **39**, 201 (1981).
[2] S. O. Unverdi and G. Tryggvason, J. Comput. Phys. **100**, 25 (1992).
[3] J. A. Sethian, *Level Set Methods* (Cambridge University Press, Cambridge, England, 1996).
[4] D. M. Anderson, G. B. McFadden, and A. A. Wheeler, Annu. Rev. Fluid Mech. **30**, 139 (1998).
[5] R. Scardovelli and S. Zaleski, Annu. Rev. Fluid Mech. **31**, 567 (1999).
[6] S. Chen and G. Doolen, Annu. Rev. Fluid Mech. **30**, 329 (1998).
[7] D. A. Wolf-Gladrow, *Lattice Gas Cellular Automata and Lattice Boltzmann Models: An Introduction* (Springer, Berlin, 2000).
[8] S. Succi, *The Lattice Boltzmann Equation for Fluid Dynamics and Beyond* (Clarendon Press, Oxford, 2001).
[9] D. Yu, R. Mei, L-S. Luo, and W. Shyy, Prog. Aerosp. Sci. **39**, 329 (2003).
[10] M. C. Sukop and D. T. Thorne, *Lattice Boltzmann Modeling: An Introduction for Geoscientists and Engineers* (Springer, Berlin, 2006).
[11] X. He and L.-S. Luo, Phys. Rev. E **56**, 6811 (1997).
[12] A. K. Gunstensen, D. H. Rothman, S. Zaleski, and G. Zanetti, Phys. Rev. A **43**, 4320 (1991).
[13] D. Grunau, S. Chen, and K. Eggert, Phys. Fluids A **5**, 2557 (1993).
[14] X. Shan and H. Chen, Phys. Rev. E **47**, 1815 (1993).
[15] X. Shan and H. Chen, Phys. Rev. E **49**, 2941 (1994).
[16] X. Shan and G. D. Doolen, J. Stat. Phys. **81**, 379 (1995).
[17] X. Shan and G. Doolen, Phys. Rev. E **54**, 3614 (1996).
[18] M. R. Swift, W. R. Osborn, and J. M. Yeomans, Phys. Rev. Lett. **75**, 830 (1995).
[19] E. Orlandini, M. R. Swift, and J. M. Yeomans, Europhys. Lett. **32**, 463 (1995).
[20] M. R. Swift, E. Orlandini, W. R. Osborn, and J. M. Yeomans, Phys. Rev. E **54**, 5041 (1996).
[21] X. He and G. D. Doolen, J. Stat. Phys. **107**, 309 (2002).
[22] X. He, X. Shan, and G. D. Doolen, Phys. Rev. E **57**, R13 (1998).
[23] X. He, S. Chen, and R. Zhang, J. Comput. Phys. **152**, 642 (1999).
[24] K. N. Premnath and J. Abraham, Phys. Rev. E **71**, 056706 (2005).
[25] A. Fakhari and M. H. Rahimian, Commun. Nonlinear Sci. Numer. Simul. **14**, 3046 (2009).
[26] A. Fakhari and M. H. Rahimian, Int. J. Numer. Methods Fluids (to be published).
[27] L.-S. Luo and S. S. Girimaji, Phys. Rev. E **67**, 036302 (2003).
[28] T. Inamuro, T. Ogata, S. Tajima, and N. Konishi, J. Comput. Phys. **198**, 628 (2004).
[29] T. Inamuro, S. Tajima, and F. Ogino, Int. J. Heat Mass Transfer **47**, 4649 (2004).
[30] R. Mei, W. Shyy, D. Yu, and L.-S. Luo, J. Comput. Phys. **161**, 680 (2000).
[31] T. Lee and C.-L. Lin, Phys. Rev. E **67**, 056703 (2003).
[32] T. Lee and C.-L. Lin, J. Comput. Phys. **206**, 16 (2005).
[33] D. Jamet, O. Lebaigue, N. Coutris, and J. M. Delhaye, J. Comput. Phys. **169**, 624 (2001).
[34] P. Yuan and L. Schaefer, Phys. Fluids **18**, 042101 (2006).
[35] H. W. Zheng, C. Shu, and Y. T. Chew, J. Comput. Phys. **218**, 353 (2006).
[36] P. L. Bhatnagar, E. P. Gross, and M. Krook, Phys. Rev. **94**, 511 (1954).
[37] S. Chen, H. Chen, D. Martinez, and W. Matthaeus, Phys. Rev. Lett. **67**, 3776 (1991).
[38] Y. H. Qian, D. d'Humières, and P. Lallemand, Europhys. Lett. **17**, 479 (1992).
[39] D. d'Humières, in *Rarefied Gas Dynamics: Theory and Simulations*, edited by B. D. Shizgal and D. P. Weave (AIAA, Washington, DC, 1992), Vol. 159, pp. 450–458.
[40] P. Lallemand and L.-S. Luo, Phys. Rev. E **61**, 6546 (2000).
[41] D. d'Humières, I. Ginzburg, M. Krafczyk, P. Lallemand, and L.-S. Luo, Philos. Trans. R. Soc. London, Ser. A **360**, 437 (2002).
[42] M. E. McCracken and J. Abraham, Phys. Rev. E **71**, 036701 (2005).
[43] S. Mukherjee and J. Abraham, Phys. Rev. E **75**, 026701 (2007).
[44] J. W. Cahn and J. E. Hilliard, J. Chem. Phys. **28**, 258 (1958).

[45] J. S. Rowlinson and B. Widom, *Molecular Theory of Capillarity* (Clarendon, Oxford, 1989).
[46] H. W. Zheng, C. Shu, and Y. T. Chew, Phys. Rev. E **72**, 056705 (2005).
[47] D. Jacqmin, J. Comput. Phys. **155**, 96 (1999).
[48] J. J. Huang, C. Shu, and Y. T. Chew, Int. J. Numer. Methods Fluids **60**, 203 (2009).
[49] V. M. Kendon, M. E. Cates, I. Pagonabarraga, J.-C. Desplat, and P. Bladon, J. Fluid Mech. **440**, 147 (2001).
[50] S. Hou, X. Shan, Q. Zou, G. D. Doolen, and W. D. Soll, J. Comput. Phys. **138**, 695 (1997).
[51] S. Chandrasekhar, *Hydrodynamic and Hydromagnetic Stability* (Clarendon Press, Oxford, 1961).
[52] R. Clift, J. R. Grace, and M. R. Weber, *Bubbles, Drops, and Particles* (Academic Press, New York, 1978).
[53] D. Bhaga and M. E. Weber, J. Fluid Mech. **105**, 61 (1981).
[54] N. Takada, M. Misawa, A. Tomiyama, and S. Hosokawa, J. Nucl. Sci. Technol. **38**, 330 (2001).
[55] D. Qian, J. B. McLaughlin, K. Sankaranarayanan, S. Sundaresan, and K. Kontomaris, Chem. Eng. Commun. **193**, 1038 (2006).
[56] A. Fakhari and M. H. Rahimian, Int. J. Mod. Phys. B **23**, 4907 (2009).
[57] K. Tsuchiya and L.-S. Fan, Chem. Eng. Sci. **43**, 1167 (1988).
[58] S. Chen, D. Martinez, and R. Mei, Phys. Fluids **8**, 2527 (1996).
[59] P. Lallemand, L.-S. Luo, and Y. Peng, J. Comput. Phys. **226**, 1367 (2007).
[60] C. Josserand and S. Zaleski, Phys. Fluids **15**, 1650 (2003).
[61] N. Baumann, D. D. Joseph, P. Mohr, and Y. Renardy, Phys. Fluids A **4**, 567 (1992).
[62] P. Lallemand and L.-S. Luo, Phys. Rev. E **68**, 036706 (2003).
[63] K. N. Premnath and J. Abraham, J. Comput. Phys. **224**, 539 (2007).